

Supplementary Information for

From Anisotropic Graphene Aerogels to Electron- and Photo-driven Phase Change Composites

Guangyong Li,^{a,b} Xuetong Zhang,^{*a} Jin Wang,^a and Jianhui Fang^{*b}

^a Suzhou Institute of Nano-tech and Nano-bionics, Chinese Academy of Sciences, Suzhou
215123, China

^b Department of Chemistry, College of Sciences, Shanghai University, Shanghai 200444, China.

*E-mail: zhangxtchina@yahoo.com (X. Zhang), jhfang@shu.edu.cn (J. Fang)

Supplementary Figures

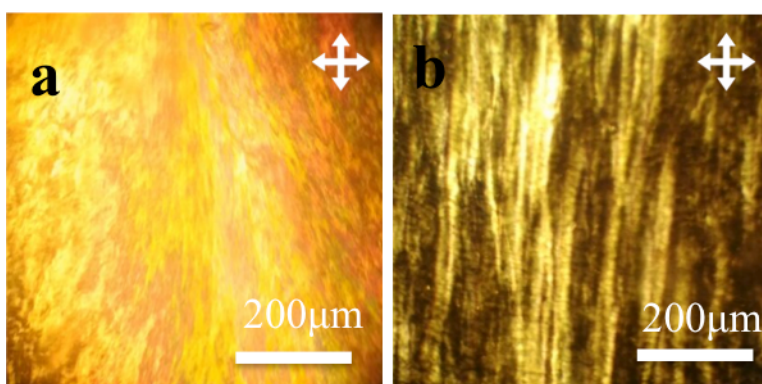


Fig. S1 Polarized-light optical microscopy (POM) images of GO-LC before and after flowing.

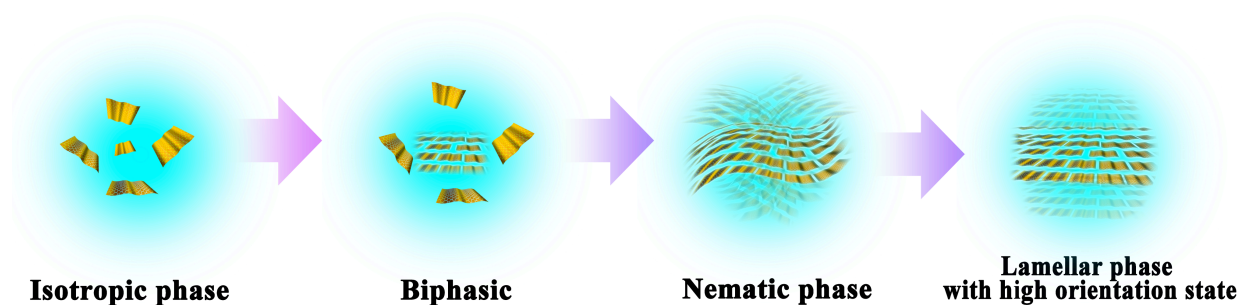


Fig. S2 The phase transition evolution of the GO dispersion with increase of the GO concentration. Under the assistance of flowing, the lamellar phase of liquid crystal can evolve to high orientational ordering with long-range arrangement.

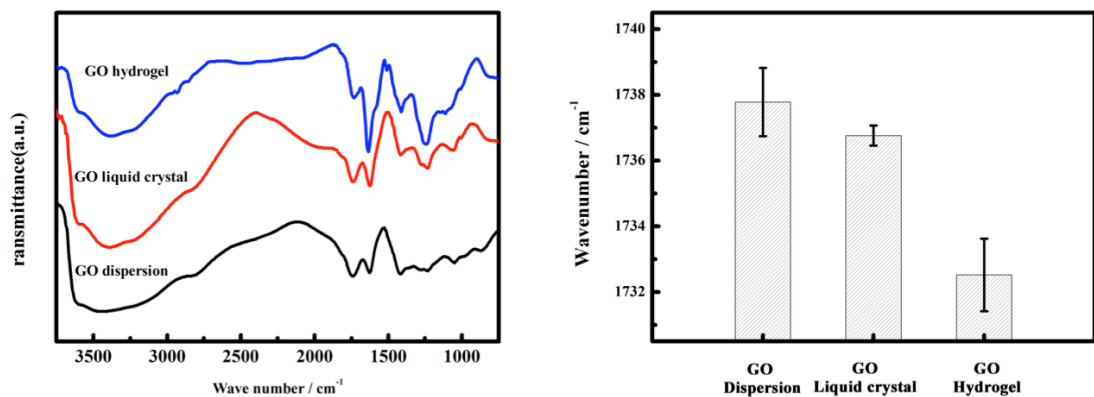


Fig. S3 Micro-IR spectra (left) of the GO dispersion, liquid crystal and hydrogen, and the wave-number distribution (right) of the C=O in Micro-IR spectra. The wave-number distribution of the C=O exhibited a downshift in comparison with GO dispersion, liquid crystal, and hydrogel. The downshift of C=O from GO-LC to GO hydrogel indicated that the generation of the hydrogen bonds between the carboxylic acid groups after HCl (g) was diffused into GO-LC. Furthermore, the downshift of C=O GO dispersion and liquid crystal due to the distance between the carboxylic acid group become shorter, the formation of hydrogen bonds become more easily.

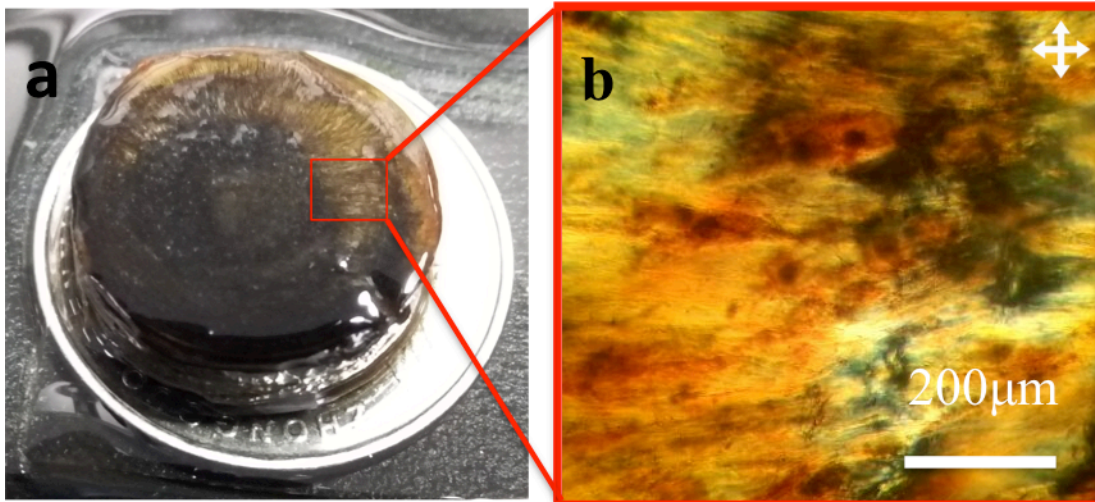


Fig. S4 Photograph and POM image of the liquid crystal GO hydrogel



Fig. S5 (a) Photographs of the AN-GOAs and (b) their cross-section planes after cutting.

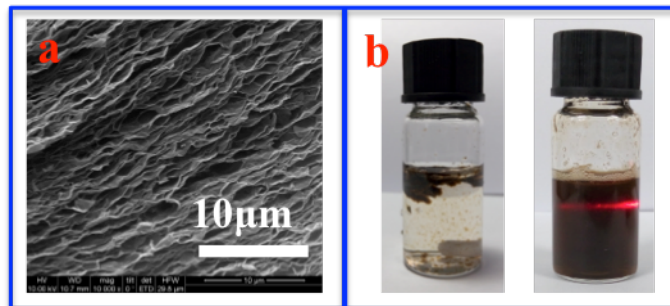


Fig. S6 (a) SEM image of the AN-GOA and (b) Photographs of the AN-GOA dissolved in water: aerogel in water (left) and the solution with Tyndall effect of AN-GOA (right).

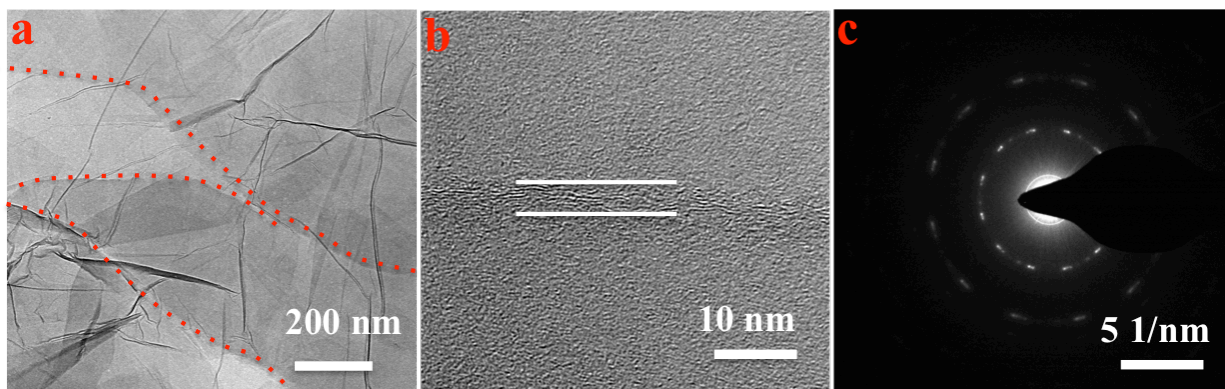


Fig. S7 TEM image (a), HR-TEM (b) image and electron diffraction pattern (c) of the AN-GOA

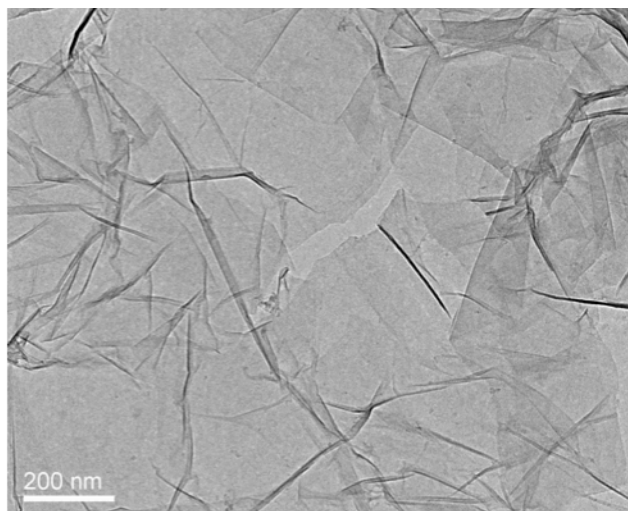


Fig. S8 TEM image of the AN-GA under low magnification

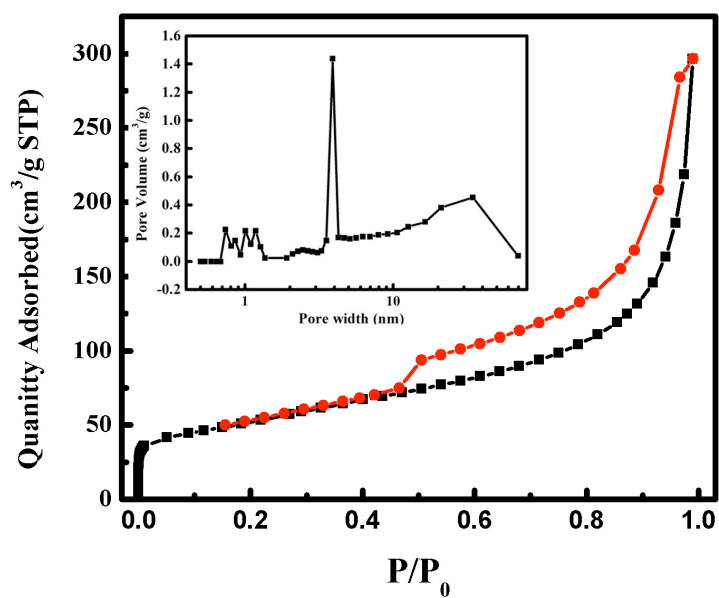


Fig. S9 Nitrogen adsorption (black square) and desorption (red circle) isotherms and the pore size distribution of the AN-GOA

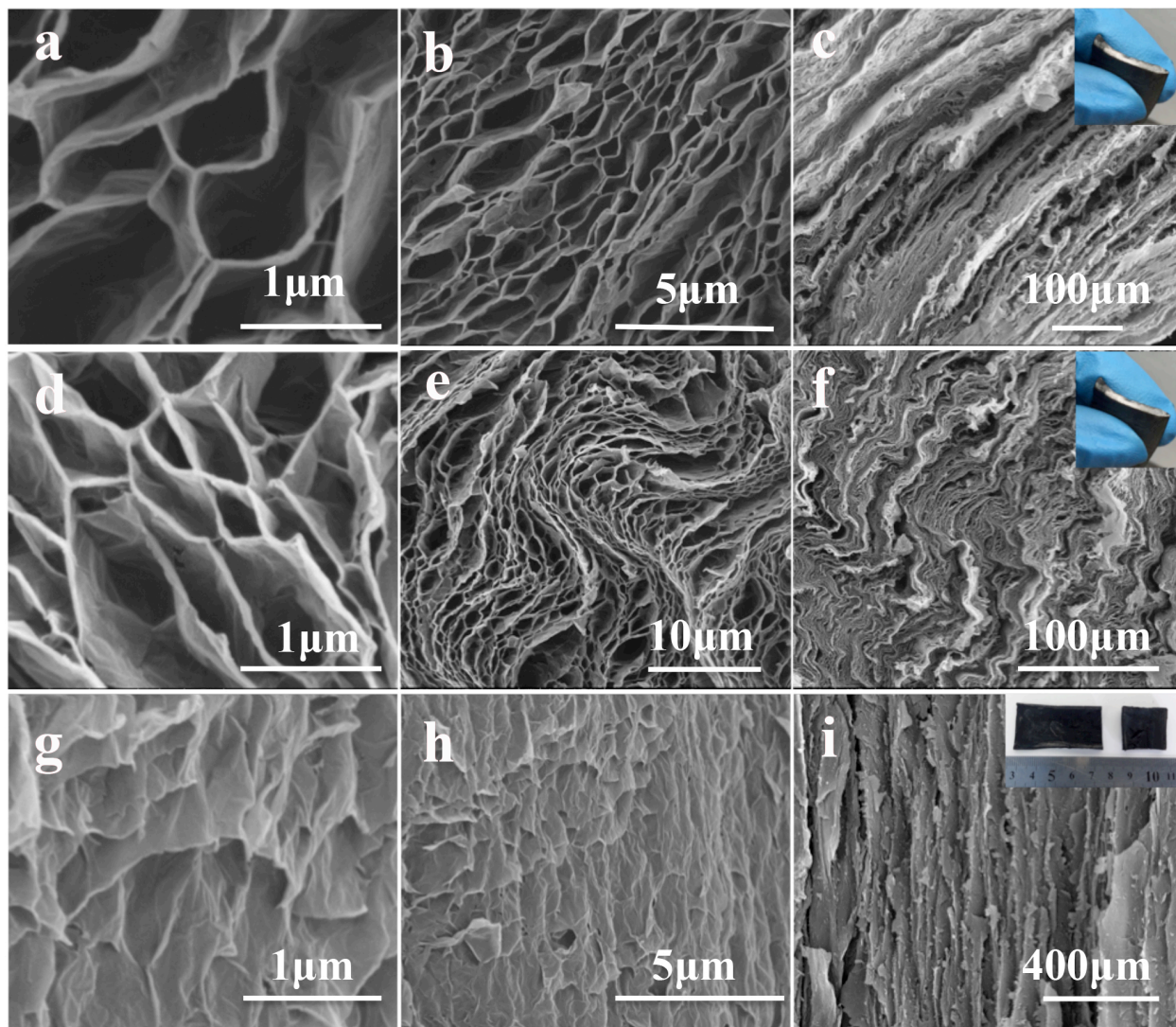


Fig. S10 SEM images of the AN-GA with rectangular shape in axial (a-f) and radial (g-i) directions

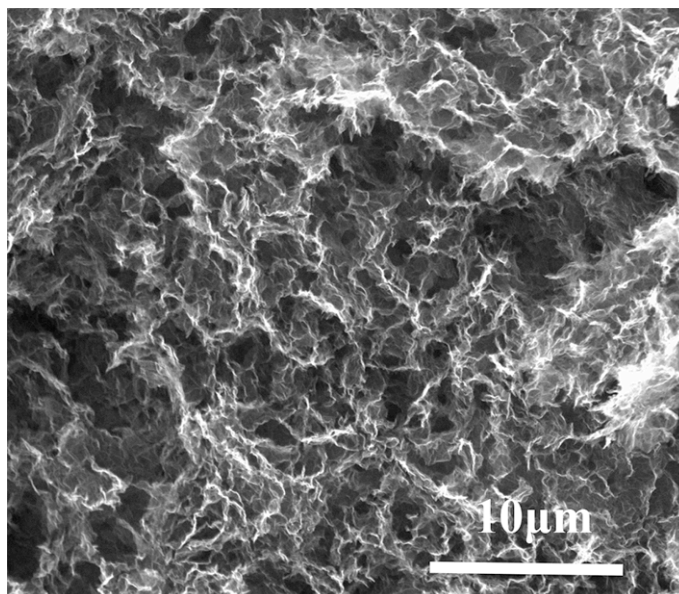


Fig. S11 SEM image of the common graphene aerogel, which prepared by chemical reduction (10wt% HI) based on the sol-gel process of GO solution

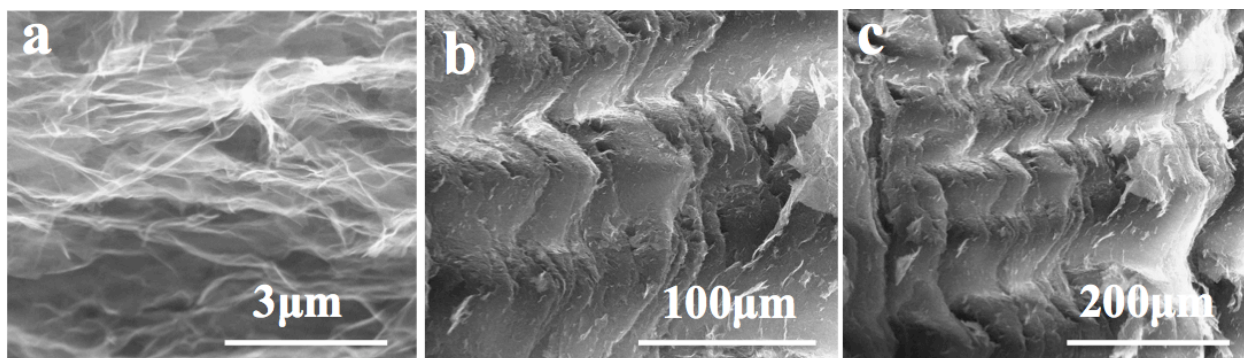


Fig. S12 SEM images of the AN-GA compressed in the axial direction.

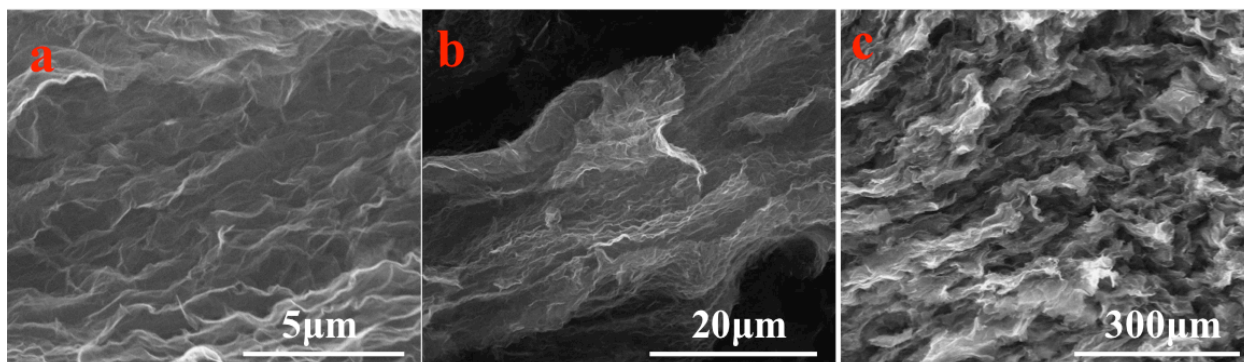


Fig. S13 SEM images of the AN-GA compressed in the radial direction.

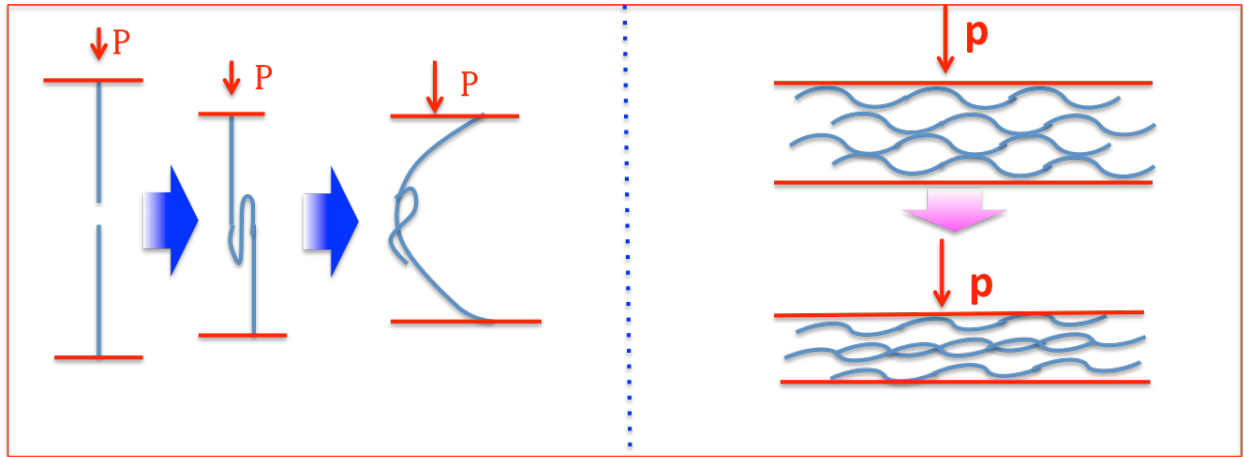


Fig. S14 Deformation mechanism of AN-GA compressed in axial (left) and radial (right) directions

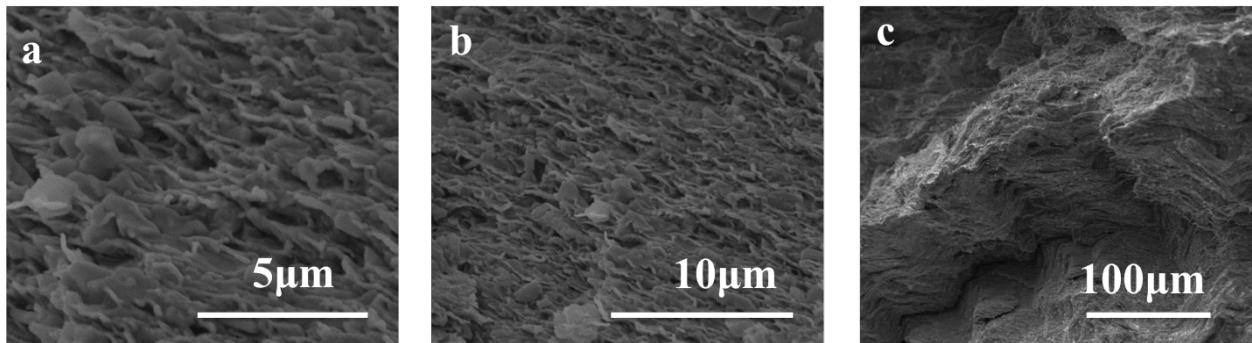


Fig. S15 SEM images of AN-GA-Paraffin under different magnification

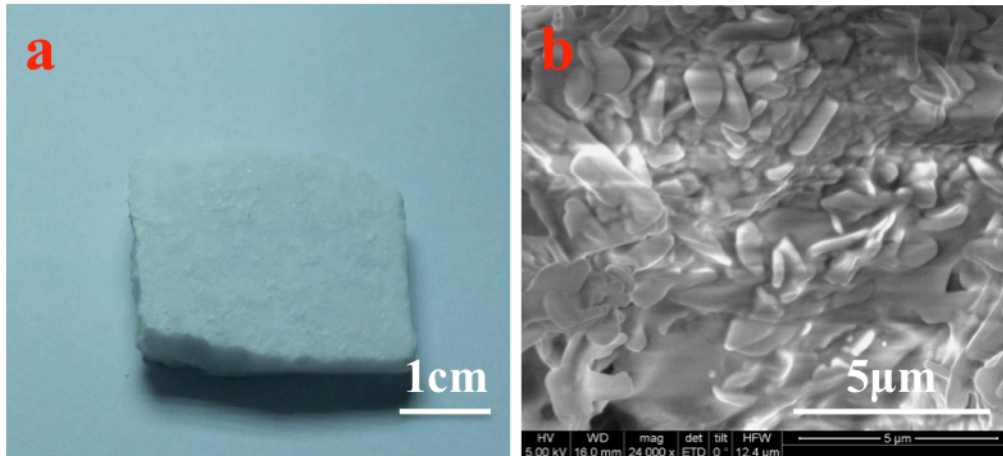


Fig. S16 Photograph and SEM image of pure paraffin

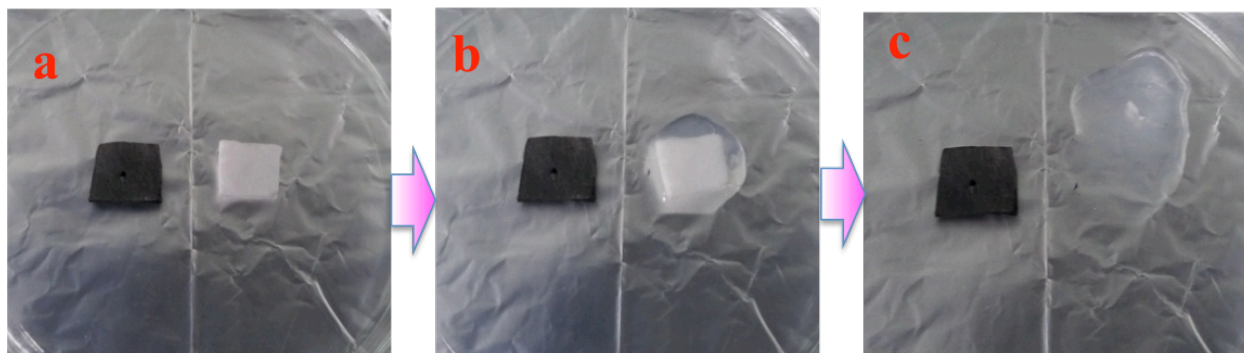


Fig. S17 The form-stability comparison of pure paraffin and AN-GA-Paraffin composite: (a) before heating, (b) during heating and (c) after heating to about 100°C

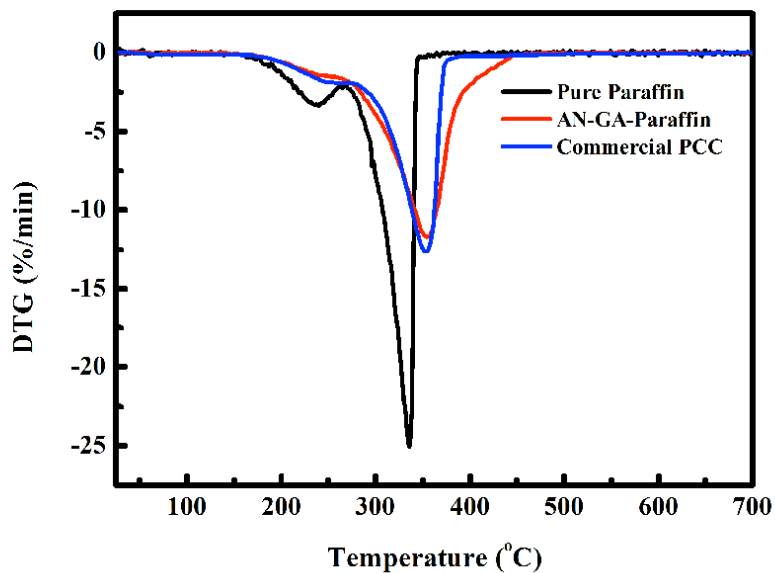


Fig. S18 DTG curves of pure paraffin, AN-GA-paraffin and commercial PCC

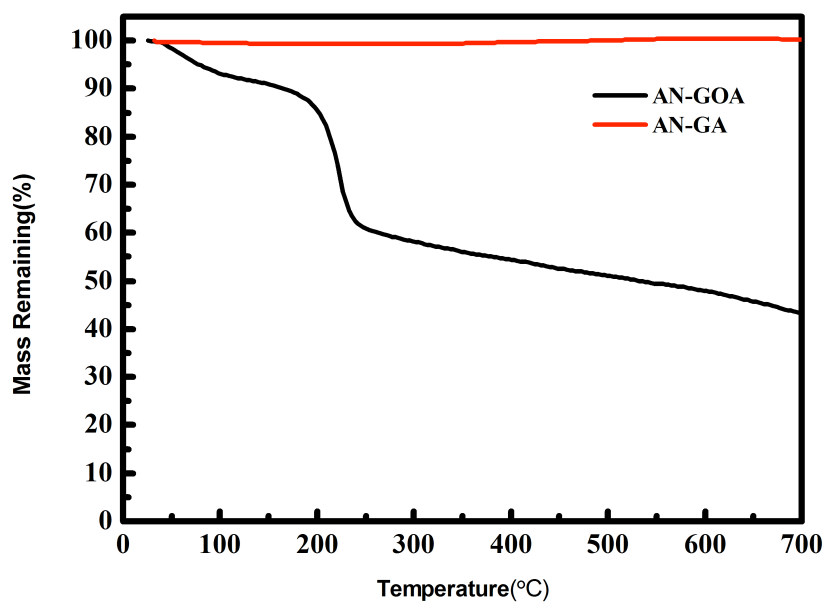


Fig. S19 TG curves of AN-GOA and AN-GA

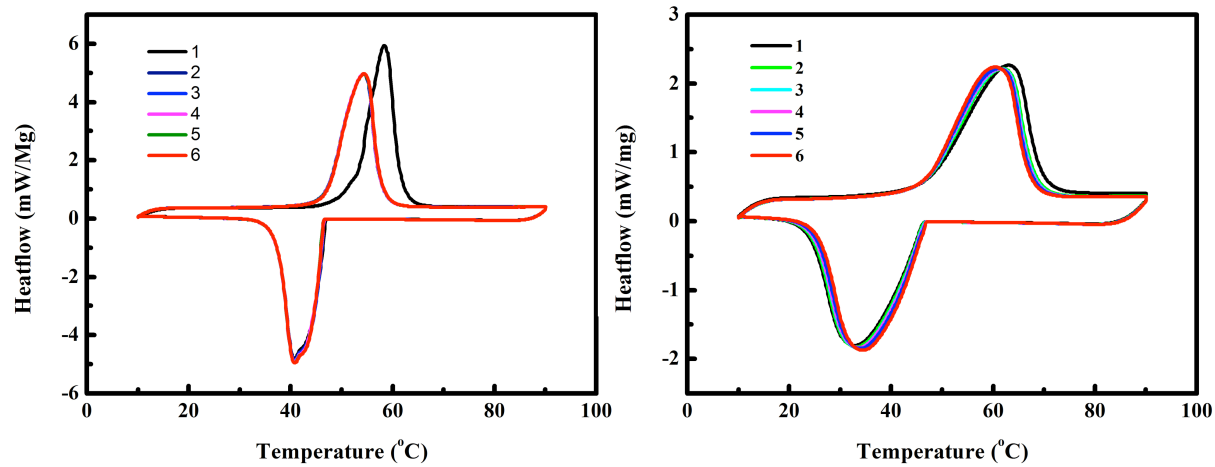


Fig. S20 DSC curves of the pure paraffin and the commercial PCC tested for 6 cycles

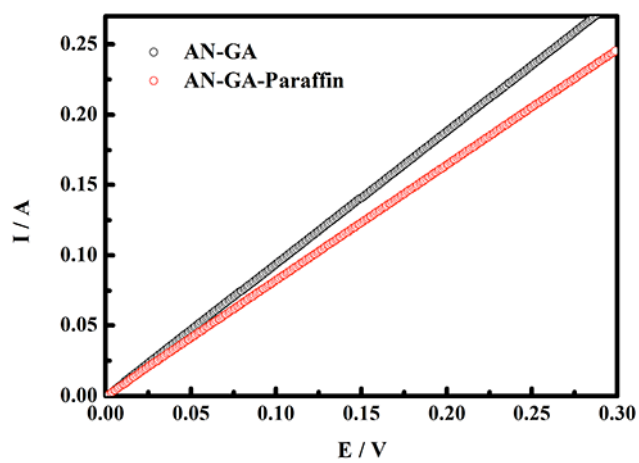


Fig. S21 I-V curves of AN-GA and AN-GA-Paraffin composite

Supplementary Tables

Table S1. The analysis of the porous structure in AN-GOA and AN-GA

Sample	Density (mg cm ⁻³)	Micropore area (m ² g ⁻¹)	Micropore area (m ² g ⁻¹)	Ratio of micropore area (%) ^{a)}	All-pore volume (cm ³ g ⁻¹)
AN-GOA	105±5	17.6	184.1	9.6	0.458
AN-GA	48±3	48.1	379.1	12.7	1.065

^{a)} The ratio of micropore area was estimated from the percentage of micropore area in BET-surface area.

Table S2. Electro-to-thermal energy storage efficiencies of AN-GA-Paraffin composites

Input voltage (V)	0.5	1.0	1.5	2.0	2.5	3
Current (A)	0.28	0.55	0.75	0.91	1.3	1.5
Start time of phase change (s)	*	142	46	27	10	7
End time of phase change (s)	*	575	195	107	44	29
Time of phase change (s)	*	433	149	80	34	22
Input energy (J)	*	238.1	167.6	145.6	110.5	99
Storage energy (J)	*	84.464	84.464	84.464	84.464	84.464
Energy storage efficiency (%) ^{a)}	*	35.5	50.5	58	76.4	85.4

^{a)} The energy storage efficiency (η) was estimated by the ratio of stored heat in paraffin, which is the total mass of paraffin enclosed in the composite (m) multiply its enthalpy (ΔH), to the received electrical energy during the phase change period, which is the product of voltage (U), current (I), and time (t). Therefore the energy storage efficiency in our system is defined as $\eta=(m\Delta H)/UIt$ assuming that all encapsulated paraffin material has participated in the phase change process.

* No melting phase change process detected

Table S3. Photo-to-thermal energy storage efficiencies of AN-GA-Paraffin composites

Light intensity (sun) ^{a)}	0.8	0.9	1.0
Start time of phase change (s)	88	65	58
End time of phase change (s)	349	242	201
Time of phase change (s)	261	177	143
Input energy (J)	49.6	37.3	34
Storage energy (J)	26.2	26.2	26.2
Energy storage efficiency (%)	52.8	70.5	77.1

^{a)} 1 sun=100 mW cm⁻², AM 1.5.